Detecting brain tumor in pathological slides using hyperspectral imaging

SAMUEL ORTEGA,[1,*] HIMAR FABELO,[1] RAFAEL CAMACHO,[2] MARÍA DE LA LUZ PLAZA,[2] GUSTAVO M. CALLICÓ,[1] AND ROBERTO SARMIENTO[1]

[1]*Institute for Applied Microelectronics (IUMA), University of Las Palmas de Gran Canaria (ULPGC), Campus de Tafira, 35017, Las Palmas de Gran Canaria, Las Palmas, Spain*
[2]*Department of Pathological Anatomy, University Hospital Dr. Negrín, Las Palmas de Gran Canaria. Barranco de la Ballena, 35010, Las Palmas de Gran Canaria, Las Palmas, Spain*
*sortega@iuma.ulpgc.es

Abstract: Hyperspectral imaging (HSI) is an emerging technology for medical diagnosis. This research work presents a proof-of-concept on the use of HSI data to automatically detect human brain tumor tissue in pathological slides. The samples, consisting of hyperspectral cubes collected from 400 nm to 1000 nm, were acquired from ten different patients diagnosed with high-grade glioma. Based on the diagnosis provided by pathologists, a spectral library of normal and tumor tissues was created and processed using three different supervised classification algorithms. Results prove that HSI is a suitable technique to automatically detect high-grade tumors from pathological slides.

References and links

1. D. N. Louis, A. Perry, G. Reifenberger, A. von Deimling, D. Figarella-Branger, W. K. Cavenee, H. Ohgaki, O. D. Wiestler, P. Kleihues, and D. W. Ellison, "The 2016 World Health Organization Classification of Tumors of the Central Nervous System: a summary," Acta Neuropathol. **131**(6), 803–820 (2016).
2. JA. F. H. Goetz, G. Vane, J. E. Solomon, and B. N. Rock, "Imaging Spectrometry for Earth Remote Sensing," Science **228**, 1147–1153 (1985).
3. G. Lu and B. Fei, "Medical hyperspectral imaging: a review," J. Biomed. Opt. **19**(1), 010901 (2014).
4. A. Bjorgan, M. Denstedt, M. Milanič, L. A. Paluchowski, and L. L. Randeberg, "Vessel contrast enhancement in hyperspectral images," in *Optical Biopsy XIII: Toward Real-Time Spectroscopic Imaging and Diagnosis*, R. R. Alfano and S. G. Demos, eds. (SPIE-Intl Soc Optical Eng, 2015).
5. H. Akbari, Y. Kosugi, K. Kojima, and N. Tanaka, "Blood vessel detection and artery-vein differentiation using hyperspectral imaging," in *Proceedings of the 31st Annual International Conference of the IEEE Engineering in Medicine and Biology Society: Engineering the Future of Biomedicine, EMBC 2009* (2009), pp. 1461–1464.
6. H. Akbari, Y. Kosugi, K. Kojima, and N. Tanaka, "Detection and analysis of the intestinal ischemia using visible and invisible hyperspectral imaging," IEEE Trans. Biomed. Eng. **57**(8), 2011–2017 (2010).
7. D. J. Mordant, I. Al-Abboud, G. Muyo, A. Gorman, A. Sallam, P. Ritchie, A. R. Harvey, and A. I. McNaught, "Spectral imaging of the retina," Eye (Lond.) **25**(3), 309–320 (2011).
8. M. Milanic, A. Bjorgan, M. Larsson, T. Strömberg, and L. L. Randeberg, "Detection of hypercholesterolemia using hyperspectral imaging of human skin," in *Clinical and Biomedical Spectroscopy and Imaging IV*, J. Q. Brown and V. Deckert, eds. (SPIE-Intl Soc Optical Eng, 2015).
9. H. Fabelo, S. Ortega, S. Kabwama, G. M. Callico, D. Bulters, A. Szolna, J. F. Pineiro, and R. Sarmiento, "HELICoiD project: a new use of hyperspectral imaging for brain cancer detection in real-time during neurosurgical operations," in *Hyperspectral Imaging Sensors: Innovative Applications and Sensor Standards 2016*, D. P. Bannon, ed. (SPIE-Intl Soc Optical Eng, 2016).
10. H. Ogihara, Y. Hamamoto, Y. Fujita, A. Goto, J. Nishikawa, and I. Sakaida, "Development of a Gastric Cancer Diagnostic Support System with a Pattern Recognition Method Using a Hyperspectral Camera," J. Sens. **2016**, 1–6 (2016).
11. Z. Liu, H. Wang, and Q. Li, "Tongue tumor detection in medical hyperspectral images," Sensors (Basel) **12**(1), 162–174 (2012).
12. H. Akbari, L. V. Halig, D. M. Schuster, A. Osunkoya, V. Master, P. T. Nieh, G. Z. Chen, and B. Fei, "Hyperspectral imaging and quantitative analysis for prostate cancer detection," J. Biomed. Opt. **17**(7), 076005 (2012).
13. Q. Ang, J. Ang, M. Hou, Q. Ingli, Y. Iting, and W. Ang, "Spectral-spatial feature-based neural network method for acute lymphoblastic leukemia cell identification via microscopic hyperspectral imaging technology,"

Biomed. Opt. Express **8**, 3017–3028 (2017).

14. J. Lou, M. Zhou, Q. Li, C. Yuan, and H. Liu, "An Automatic Red Blood Cell Counting Method Based on Spectral Images," Image and Signal Processing **2016**, 1391–1396 (2016).

15. C. Lu and M. Mandal, "Toward Automatic Mitotic Cell Detection and Segmentation in Multispectral Histopathological Images," IEEE J. Biomed. Health Informatics **18**, 594–605 (2014).

16. S. Ortega, H. Fabelo, R. Camacho, M. L. Plaza, G. M. Callico, R. Lazcano, D. Madroñal, R. Salvador, E. Juárez, and R. Sarmiento, "P03.18 Detection of human brain cancer in pathological slides using hyperspectral images," Neuro-oncol. **19**(suppl_3), iii37 (2017).

17. D. N. Louis, H. Ohgaki, O. D. Wiestler, W. K. Cavenee, P. C. Burger, A. Jouvet, B. W. Scheithauer, and P. Kleihues, "The 2007 WHO Classification of Tumours of the Central Nervous System," WHO **2007**, 97–109 (2007).

18. E. E. Holt, M. Aikio, and V. teknillinen tutkimuskeskus, *Hyperspectral Prism-Grating-Prism Imaging Spectrograph*, VTT Julkaisuja (Technical Research Centre of Finland, 2001).

19. S. Ortega, G. M. Callico, M. L. Plaza, R. Camacho, H. Fabelo, and R. Sarmiento, "Hyperspectral database of pathological in-vitro human brain samples to detect carcinogenic tissues," in *Proceedings - International Symposium on Biomedical Imaging* (2016), Vol. 2016–June.

20. A. Plaza, J. Atli, J. W. Boardman, J. Brazile, L. Bruzzone, G. Camps-valls, J. Chanussot, M. Fauvel, P. Gamba, A. Gualtieri, M. Marconcini, J. C. Tilton, and G. Trianni, "Remote Sensing of Environment Recent advances in techniques for hyperspectral image processing," Remote Sens. Environ. **113**, S110–S122 (2009).

21. J. A. Richards, *Remote Sensing Digital Image Analysis* (Springer Berlin Heidelberg, 2012).

22. R. Gillies, J. E. Freeman, L. C. Cancio, D. Brand, M. Hopmeier, and J. R. Mansfield, "Systemic Effects of Shock and Resuscitation Monitored by Visible Hyperspectral Imaging," Diabetes Technol. Ther. **5**(5), 847–855 (2003).

23. S. Lopez, "A Novel Use of Hyperspectral Images for Human Brain Cancer Detection using in-Vivo A Novel Use of Hyperspectral Images for Human Brain Cancer," BIOSIGNALS 311–320 (2016).

24. J. Burger and A. Gowen, "Data handling in hyperspectral image analysis," Chemom. Intell. Lab. Syst. **108**(1), 13–22 (2011).

25. P. Ghamisi, J. Plaza, Y. Chen, J. Li, and A. J. Plaza, "Advanced Spectral Classifiers for Hyperspectral Images: A review," IEEE Geosci. Remote Sens. Mag. **5**(1), 8–32 (2017).

26. G. Camps-Valls and L. Bruzzone, "Kernel-based methods for hyperspectral image classification," IEEE Trans. Geosci. Remote Sens. **43**(6), 1351–1362 (2005).

27. Q. Li, X. He, Y. Wang, H. Liu, D. Xu, and F. Guo, "Review of spectral imaging technology in biomedical engineering: achievements and challenges," J. Biomed. Opt. **18**(10), 100901 (2013).

28. R.-E. Fan, K.-W. Chang, C.-J. Hsieh, X.-R. Wang, and C.-J. Lin, "LIBLINEAR: A Library for Large Linear Classification," J. Mach. Learn. Res. **9**, 1871–1874 (2008).

29. J. A. Benediktsson, J. A. Palmason, and J. R. Sveinsson, "Classification of hyperspectral data from urban areas based on extended morphological profiles," IEEE Trans. Geosci. Remote Sens. **43**(3), 480–491 (2005).

30. H. Akbari, Y. Kosugi, K. Kojima, and N. Tanaka, "Wavelet-Based Compression and Segmentation of Hyperspectral Images in Surgery," in *Lecture Notes in Computer Science* (Springer Nature, n.d.), pp. 142–149.

31. F. Blanco, M. López-Mesas, S. Serranti, G. Bonifazi, J. Havel, and M. Valiente, "Hyperspectral imaging based method for fast characterization of kidney stone types," J. Biomed. Opt. **17**(7), 076027 (2012).

32. T. G. Dietterich, "Ensemble Methods in Machine Learning," in *Multiple Classifier Systems* (Springer Nature, 2000), pp. 1–15.

33. J. C.-W. Chan and D. Paelinckx, "Evaluation of Random Forest and Adaboost tree-based ensemble classification and spectral band selection for ecotope mapping using airborne hyperspectral imagery," Remote Sens. Environ. **112**(6), 2999–3011 (2008).

34. H. Akbari, L. V. Halig, H. Zhang, D. Wang, Z. G. Chen, and B. Fei, "Detection of cancer metastasis using a novel macroscopic hyperspectral method," in *Progress in Biomedical Optics and Imaging - Proceedings of SPIE* (2012), Vol. **8317**.

35. G. Lu, L. Halig, D. Wang, Z. G. Chen, and B. Fei, "Spectral-Spatial Classification Using Tensor Modeling for Cancer Detection with Hyperspectral Imaging.," Proc. SPIE–the Int. Soc. Opt. Eng. **9034**, 903413 (2014).

36. R. Pike, G. Lu, D. Wang, Z. G. Chen, and B. Fei, "A Minimum Spanning Forest-Based Method for Noninvasive Cancer Detection With Hyperspectral Imaging," IEEE Trans. Biomed. Eng. **63**(3), 653–663 (2016).

1. Introduction

Prior to the release of the 2016 World Health Organization (WHO) Classification of Tumors of the Central Nervous System (CNS), the diagnosis and classification of brain tumors were solely based on the histological analysis of tissue [1]. According to this criterion, the diagnosis relies in the examination of specimens by searching for microscopic features of tissue in Hematoxylin and Eosin (H&E) stained sections. Although the current WHO classification of tumors of CNS employs both the histological and the molecular analysis of tissue to provide a diagnostic, in this paper we explore the use of a novel technology in the

medical field, hyperspectral imaging (HSI), as a complementary tool for detecting tumor during the examination of pathological slides.

Hyperspectral Imaging, also known as imaging spectroscopy [2], is a technology capable of acquiring hundreds of contiguous spectral bands for a given scene. The interest of this imaging technique is given by the fact that the interaction between the electromagnetic radiation of light with a certain material is singular for that specific material. The measured spectrum from a material is called spectral signature or spectral fingerprint. Through the analysis of this wavelength-dependent function it is possible to discriminate between different types of materials. The biological and pathological changes in tissues and organs have a close relationship with the spectra. Spectral characteristics in different wavelength regions yield a distinguishable spectral signature, making pathological changes identifiable. Therefore, the interaction between the electromagnetic radiation and tissue carries quantitative information about tissue pathology [3].

For these reasons, HSI is an emerging technology in the medical field. In the recent years, many researchers have explored this technology as a diagnostic aid tool for different applications. Compared to other existing technologies for assessing the diagnosis, one of the strengths offered by HSI is being completely non-invasive. In biomedical applications, this technology has been employed in a wide range of disciplines, including blood vessel visualization enhancement [4,5], intestinal ischemia identification [6], measuring the oximetry of the retina [7], estimating of the cholesterol levels [8] or cancer detection [9–12], among others. Regarding pathological analysis of hyperspectral (HS) data, the number of studies available in the literature is limited. Some examples are the identification of acute lymphoblastic leukemia [13], blood cell analysis [14] or mitotic cell detection and segmentation [15].

In this research work, HS data from pathological slides belonging to human brain tissue suffering high-grade gliomas have been analyzed. The main goal of this study is to analyze if it is possible to discriminate between normal and tumor tissue in pathological slides by processing only their spectral information. To this end, HS data have been processed using a supervised classification framework. Three different classifiers have been employed to automatically distinguish between tumor and normal tissue, using as features only the spectral information of the tissues. A qualitative description of this methodology has been recently published [16].

2. Materials and methods

The experiments carried out in this research work were performed employing hyperspectral images obtained from in-vitro human brain tissue pathological slides, using a custom microscopic hyperspectral acquisition system. Then, data were processed with three different machine-learning algorithms to classify and identify the tissue samples. In this section, the materials and methodology employed to achieve the proposed goals of distinguishing tissue samples by its spectral characteristics are detailed.

2.1. Biological samples

The biological samples used in this research work consisted of biopsies of human brain tissue resected during surgery that followed a histological process, whereby tissue specimens were prepared for sectioning, staining and diagnosis. Twenty-one diagnosed pathological slides obtained from ten different patients affected by grade IV glioblastoma tumor were included in this study (Fig. 1(a)). The examination of the biopsy under a microscope is the conclusive way that a brain tumor can be trustworthy diagnosed by a pathologist. These pathological slides were provided by the Pathological Anatomy department of the University Hospital Doctor Negrín at Las Palmas of Gran Canaria (Spain). The study protocol and consent procedures were approved by the Comité Ético de Investigación Clínica-Comité de Ética en la Investigación (CEIC/CEI) of the same hospital. Once biopsy was diagnosed, tissue is

identified according to the World Health Organization (WHO) classification of tumors of the nervous system [17]. In order to facilitate the labelling process of the HS data, after pathologists determined the diagnosis of a certain tissue, the regions of interest in each slide were highlighted using a colored pen. Tumor tissue were marked using red color, while normal tissue were marked using blue color (Fig. 1(b) and 1(c)).
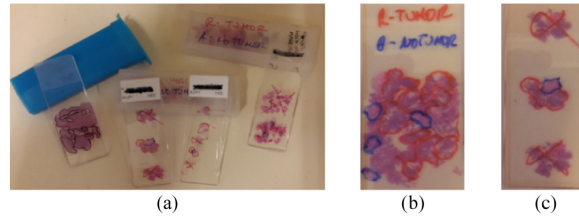

Fig. 1. Biological samples. (a) Pathological slides overview. (b) and (c) Diagnosed pathological slides with the tumor and normal tissue surrounded by red and blue color respectively.

2.2. Acquisition system

In order to register HS images from pathology slides, a customized microscopic HS acquisition system was developed. The system is formed by a HS pushbroom camera coupled to an optical microscope with a customized scanning platform for the pathological slides based on a linear actuator (Fig. 2(a)). The HS camera employed is a Hyperspec VNIR A-Series from HeadWall Photonics, which is based on a PGP (prism-grating-prism) [18] spectrometer coupled to a CCD (Charge-Coupled Device) sensor. This HS system works in the spectral range from 400 nm to 1000 nm (VNIR) with a spectral resolution of 2.8 nm, being able of sampling 826 spectral channels. This HS camera is based on a pushbroom scanning, so to capture a whole HS cube (containing both the spectral and spatial information from a scene) either the camera or the sample must be moved synchronously with the camera trigger. The microscope used is the Olympus BH2-MJLT. Using this microscope, it is possible to perform observations by transmittance or reflectance of light with magnifications of 5x, 10x, 20x, 50x and 100x. The microscope includes a light source that consists in a power adjustable halogen bulb (Philips CAPSUline PRO 13102) capable of bringing a broadband emission in the range between 400 nm to 1000 nm.
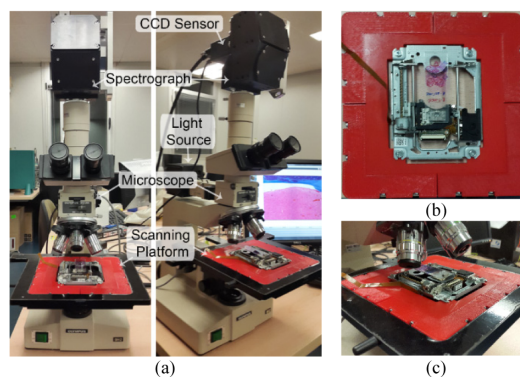

Fig. 2. Microscopic HS acquisition system. (a) System overview modified for HIS acquisition. (b) Designed flat base of the scanning platform. (c) Scanning platform attached to the microscope.

So as to obtain a HS cube from the pathological slides, a customized scanning platform based on a linear-movement mechanism with a resolution of 4.5 μm was developed. The scanning platform was attached to the microscope employing a customized 3D-printed flat

base, which replaces the original plate of the microscope (Fig. 2(b)). For a 5x magnification, each pixel represents an area of 1.32×1.32 mm, while the movement resolution of the linear mechanism is limited to 4.5 μm. The lower resolution of the linear mechanism compared to the pixel resolution of the optical system impose a limitation in the spatial information that can be collected to create a HS cube. This fact implies that a complete pathological slide cannot be captured in a single shot, because there is a spatial information gap between the contiguous lines that compose the HS cube.

2.3. Hyperspectral database

Employing the previously described microscopic HS acquisition system, the spectral database described in [19] was obtained. This database consists of 36 HS cubes collected using a 5x magnification. Each hyperspectral cube is composed by 826 spectral channels and 1004×600 pixels. Figure 3(a) and 3(b) show the synthetic RGB representations of two different HS cubes captured from pathological slides presenting tumor and healthy tissue respectively. As previously mentioned, tissue inside red markers were diagnosed as tumor while tissue inside blue marker were diagnosed as normal tissue.

As indicated in the description of the HS acquisition system, not all the full spatial information can be captured by this HS camera. If the full spatial information would be available, the morphological characteristics of the tissue could be exploited, employing similar criteria of that used by pathologists for diagnosing (i.e. cell proliferation and nuclei morphology). Figure 3(c) shows a typical histological image used by pathologist to diagnose brain tumor. Compared with Fig. 3(a) or 3(b), it can be seen that the histological image allow distinguishing cells, what is not possible in the acquired HS images. This spectral information consists of a mixture of all tissues inside a certain area of a pathological slide. Nevertheless, in real applications, different regions of a tissue could have different spectrum. Although we would like to isolate the different elements in a pathological slide, i.e. cells, our scanning system constraints the spatial resolution of the images. For this reason, in this research study all the tissue inside an area is macroscopically extracted for the classification. Due to this fact, in this study only the spectral information obtained from the HS cubes has been taken into account. Furthermore, the objective of this research work is to analyze if solely the spectral signature analysis is a useful complementary tool for detecting brain tumor in pathological slides, as the morphological analysis has been already proven to be appropriate to this end.
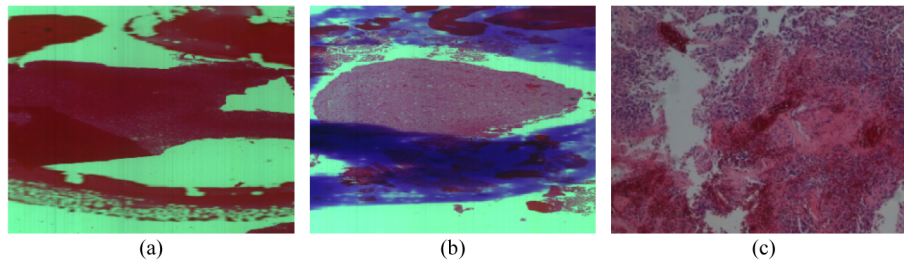

(a)　　　　　　　　(b)　　　　　　　　(c)

Fig. 3. Synthetic RGB representations of a HS cube acquired from a pathological slide of (a) tumor tissue and (b) normal tissue. (c) Histological image of a brain tissue sample (100x).

As it will be detailed next in the pre-processing chain description section, a region of interest (ROI) of each HS cube were defined to extract a spectral signature data set. In this study, two different classes of tissue have been defined: tumor tissue and normal tissue. Table 1 summarizes the labelled data set of spectral signatures available for each patient per tissue class after defining the ROI and extracting the spectral data from each hypercube. The spectral signatures for both classes and all patients are shown on Fig. 4. These spectral signatures have been calculated as the mean spectrum of each tissue type for each patient. The spectral signatures depicted in blue lines belong to normal tissue and the ones depicted in red

lines belong to tumor tissue. After a visual inspection of these spectral signatures, it can be noticed that there are significant differences between the signatures of normal and tumor tissue, especially in the spectral range between 550 nm and 700 nm.

Table 1. Spectral signature labelled data set summary

#Patient	#Total of spectral samples	
	Normal	Tumor
P1	36,648	36,685
P2	36,923	37,826
P3	35,159	35,181
P4	36,821	37,800
P5	37,321	35,230
P6	35,366	37,379
P7	36,605	37,718
P8	36,736	38,242
P9	-	38,325
P10	-	39,399
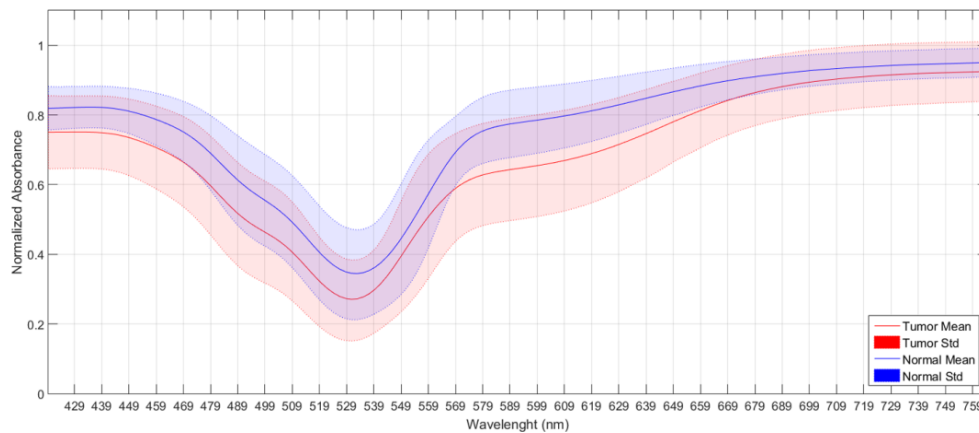
Fig. 4. Average spectral signatures of tumor tissue (red) and normal tissue (blue) and their respective standard deviation.

2.4. Processing framework

The proposed processing framework is based on a supervised classification scheme. Although it has been proven that combining both the spatial and spectral features of the hyperspectral images can improve the accuracy in the predictions [20], in this research work only the spectral characteristics of the data have been taken into account. In future works it will be interesting to combine both sources of information once the suitability of the spectral analysis has been proven. The inputs of the classifiers are the measured spectral signatures from healthy and tumor pixels. Figure 5 shows an overview of the processing framework employed in this study. The first stage of the proposed framework consists of a pre-processing chain that aims to compensate the effects produced by the environmental conditions and the sensor response of the acquisition system during the capture procedure of the HS cubes. Then, a supervised classification is performed using three different classification methods. Finally, the performance of the classifiers is evaluated using standard metrics for assessing a classifier performance.
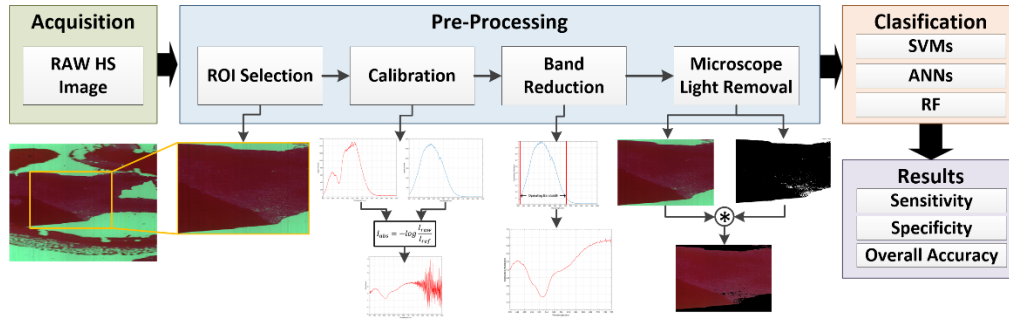
Fig. 5. Processing framework block diagram.

2.4.1. Data preprocessing

The pre-processing chain proposed in this research work is based on four steps: 1) selection of the ROI; 2) image calibration; 3) spectral band reduction; and 4) removal of the microscope light inside the pathological slide where there is no tissue sample. Following, each step of the pre-processing chain is explained.

1) **ROI selection:** First, due to the high dimensionality of the HS cubes, which extremely slows down the processing of the data, a manual ROI selection is applied. In this procedure, the ROI selection is carefully performed taking a ROI that is a balanced solution between selecting a reduced area (that involves decreasing the computational cost) and choosing enough relevant data inside each area.

2) **Calibration:** The second stage of the preprocessing chain is related to the calibration of the image. Through the calibration, the acquired image is transformed from radiance observation to absorbance. The absorbance image (I_{abs}) is calculated by taking the ratio between the raw HS image (I_{raw}) with respect to a reference image (I_{ref}) Eq. (1). This is a standard procedure for hyperspectral images [21]. The reference material provides a measure of the instrument response function from the resultant optical density image set [22]. Figure 6(a) shows a single spectral signature extracted from the raw data acquired by the HS camera while Fig. 6(b) shows the reference spectrum of the microscope light, passing through an empty pathological slide, acquired by the HS camera. Finally, the calibrated spectrum in absorbance mode is shown in Fig. 6(c).
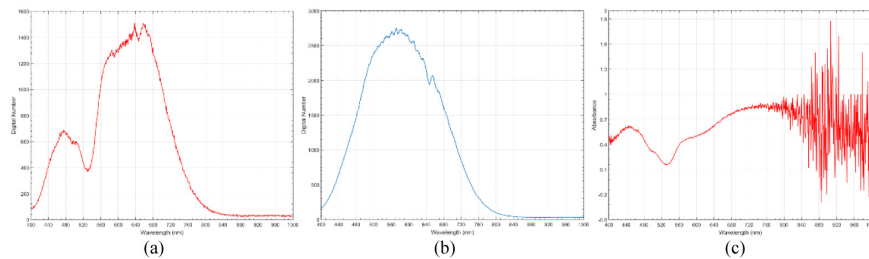
$$I_{abs} = -log \frac{I_{raw}}{I_{ref}} \tag{1}$$

Fig. 6. Spectral signatures of a single tumor pixel in each calibration step. (a) Raw spectrum. (b) Reference spectrum. (c) Calibrated spectrum.

3) **Band reduction:** The next stage in the pre-processing chain performs a band reduction of the HS cube since there are spectral channels that do not carry any relevant information. In the reference spectrum presented in Fig. 6(b), it can be seen that the measured intensity is almost zero for the extreme wavelengths (mainly produced because the microscope is not optimized to be employed beyond the limits of the visible spectral range), so these bands can be removed to avoid the inclusion of meaningless information in the machine learning scheme. The selected operating bandwidth covers the spectral range from 419 nm to 768 nm (Fig. 7(a)), which has demonstrated to be a meaningful range across all the spectra. Furthermore, the measured spectral signatures present high redundancy between contiguous bands due to the high resolution of the HS camera sensor related with the diffraction capability of the optical grating. The spectral resolution of the HS camera is 2.8 nm, obtaining 826 spectral bands, so each contiguous band is sampled at 0.6 nm approximately, thus producing redundant information. In order to avoid this redundancy and to reduce the dimensionality of the HS cubes (to accelerate the processing of the samples), the spectral bands were averaged in a similar way as proposed in [23]. The spectral signature generated after applying the band average can be observed in Fig. 7(b). It can be observed that the overall shape of the spectral signature does not change compared with the full-spectra signature, with 826 spectral channels (Fig. 6(c)).
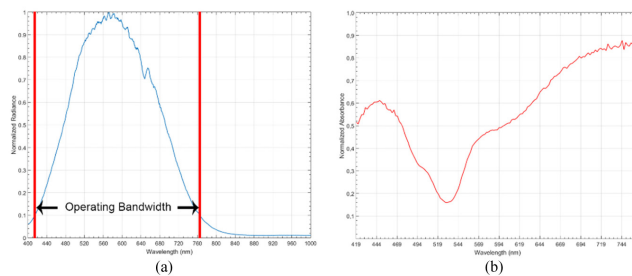

Fig. 7. Spectral signatures of a single pixel in the band reduction step. (a) Selected operating bandwidth in the reference spectrum. (b) Calibrated spectral signature after the spectral band reduction.

4) **Microscope light removal:** Finally, in order to process only the useful information of the HS cube, a method to discriminate between pixels that belong to the microscope light were developed. This method is based on a binarization process performed over the synthetic RGB image extracted from the HS cube, taking advantage of the white color of the measured light. After a manual selection of the suitable threshold for binarizing the image, it is possible to isolate the microscope light to avoid processing light pixels without relevant information. Figure 8(a) shows the synthetic RGB representation of a HS cube acquired from a healthy pathological slide before the binarization process. Figure 8(b) shows the binarized images and Fig. 8(c) the synthetic RGB representation after removing the pixels associated with the microscope light.
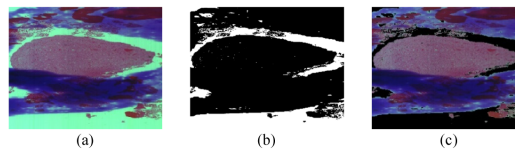

Fig. 8. Synthetic RGB representations of a HS cube acquired from a healthy area of pathological slide. (a) Synthetic RGB image without light pixels removal. (b) Binarized image. (c) Synthetic RGB image after the binarization process application to remove light pixels.

2.4.2. Supervised classification

An extensive literature about pixel-wise classification of HS images is available in the current state-of-the-art. When using this technique, each pixel of a HS cube is assigned to a certain class based exclusively on its spectral signature analysis. For this purpose, approaches based on decision trees, neural networks and kernel-based methods have been widely used. These algorithms have to face two main problems: the high dimensionality of data and the limited size of sample data [24]. The supervised algorithms employed in this research work have been Support Vector Machines (SVMs), Artificial Neural Networks (ANNs) and Random Forest (RF). In a recent review article [25], these classifiers have been highlighted among others, such as Multinomial Logistic Regression (MLR) or Deep Learning techniques, for the pixel-wise classification of hyperspectral images. Nevertheless, in this study we only analyses SVM, ANNs and RF as they have been shown to be more computationally efficient.

SVMs are kernel-based supervised classifiers that have been widely used in the classification of HS images. In the literature, it is shown that SVMs achieve good performance for classifying HS data, even when a limited number of training samples are available [26]. Due to its strong theoretical foundation, good generalization capabilities, low sensitivity to the curse of dimensionality, and ability to find global classification solutions, many researchers usually prefer SVMs instead of other classification algorithms for classifying HS images [27]. In this research work, the LIBLINEAR [28] integrated software for support vector classification has been used.

Recent remote sensing literature has shown that SVM methods generally outperform traditional statistical analysis based on ANN methods in classification problems involving HS images. Nevertheless, ANNs have been also successfully employed in the classification of HS images [26,29]. Some studies have applied ANNs as classifiers over HS images in the medical field [30,31]. The ANN used in this research work is a feed forward Multilayer Perceptron (MLP) network, trained using a backpropagation algorithm. The MATLAB Neural Network Toolbox has been selected to test the quality of these algorithms in the classification of in-vitro hyperspectral brain tissue.

Finally, the third algorithm tested in this supervised classification approach is Random Forest. RF is an ensemble classification algorithm that builds a set of classifiers and classify new data by performing a voting of their predictions [32]. Several studies have demonstrated that these ensemble methods can provide a classification result as accurate as other traditional classifiers, like ANNs [33]. In order to test this supervised ensemble algorithm in the classification of HS pathological data, the MATLAB Machine Learning Toolbox has been employed.

2.4.3. Evaluation metrics

The results obtained by the supervised classifiers were evaluated using the standard sensitivity, specificity and overall accuracy (OA) metrics. These are frequently employed as statistical measures of the performance of hyperspectral image classification [34–36]. Sensitivity is related to the tests ability to identify a condition correctly. It is obtained as the number of true positives (TP) divided by the total number of true positives and false negatives (FN) in a population Eq. (2). Specificity is related to the tests ability to exclude a condition correctly. It is obtained as the number of true negatives (TN) divided by the total number of true negatives and false positives (FP) in a population Eq. (3). Finally, overall accuracy is calculated by dividing the total number of successful results by the total population Eq. (4).

$$Sensitivity = \frac{TP}{TP + FN} \tag{2}$$

$$Specificity = \frac{TN}{TN + FP} \tag{3}$$

$$OA = \frac{TotalSuccess}{TotalPopulation} \qquad (4)$$

2.5. Experiment description

In order to validate supervised classification algorithms for discriminating between normal and tumor tissue, three different case studies (CSs) have been proposed. This approaches differs in which patients are included as subject of study. These scenarios are described below:

- **Case study 1 (CS1):** The goal of this CS is to check if the discrimination between normal and tumor tissue can be performed using the available labelled data, avoiding the inter-patient variability of data. The data sets explored in this CS include HS cubes from pathological slides where both type of tissue, normal and tumor, are present. In order to avoid the inter-patient variability of data, data from each patient is used independently for training and testing the supervised classifiers. Patients #9 and #10 are not included in this CS because no normal samples are available from these two patients.

- **Case study 2 (CS2):** In CS2, all the available labelled data are merged into a unified data set, taking into account the inter-patient variability in this scenario. All the samples for the ten patients have been included in this CS.

- **Case study 3 (CS3):** This case study is the most realistic one in a diagnosis context. In this scenario, each patient data are used independently as a test set for the classification algorithm. The classifier model is trained by using the information from the rest of the HS labelled data that belong to the remaining patients. This CS represents a real case where new samples arrive to the pathological laboratory and the classification must be performed using a classifier trained with data from previous patients.

In this research work, a 10-fold cross-validation (CV) was used as model validation scheme for CS1 and CS2, randomly partitioning the data set in 10 folds and using only one fold for training the classifier (10% of data) and the remaining data are used to assess the classifier performance. The process is repeated until each fold has been used to train the classifier, and finally the classifier performance is calculated as the average of the performance obtained in each iteration. In CS3, it is not possible to apply cross-validation, so the model was evaluated using hold-out validation, where the test set corresponds to the spectral samples from one patient, and the classifier is trained using all the available spectral signatures from the remaining patients.

3. Experimental results

This section presents the results achieved after applying the supervised classification framework described in section 2 to the in-vitro human brain hyperspectral data set. These results present the performance estimation of each classifier for each CS. In addition, the computational cost of each classifier is shown as a measure of the time required to train and evaluate the performance of each classifier, employing a computer with Intel Core i7-4770k at 3.5GHz.

Three different supervised classifiers were evaluated: SVMs, ANNs and RF. A linear kernel has been tested in the SVM classifier. Several ANN topologies were tested, (varying the number of hidden layers, the number of neurons inside each layer and the activation function selected for each layer). The selected ANN topology consists of a multilayer neural network with two hidden layers composed by 36 and 16 neurons respectively (employing a logistic activation function for these layers) and using a hyperbolic tangent sigmoid activation function for the output layer. After simulating the classifier using different network

topologies, it has been experimentally determined that this architecture is the most suitable for this application. Finally, an ensemble of 50 different classification trees composes the RF configuration. It has been detected that the use of an increased number of classification trees does not improve the classification accuracy.

3.1. Case study 1

As commented before, CS1 implies the classification of data that only belongs to a single patient. For this reason, due to the absence of normal tissue for patient #9 and #10, these patients were not included in this experiment. The estimation of the model performance was obtained using 10-fold cross-validation. Table 2 shows the classification results obtained for each classifier per patient in this CS.

It can be seen that the results achieved employing the SVM classifier offers a competitive discrimination between normal and tumor tissue with high sensitivity and specificity (higher than 90% in any case). On the other hand, the results obtained using ANNs outperform 93% of overall accuracy for every patient, being the most suitable classifier for this CS. In terms of specificity and sensitivity, these results show a good discrimination rate between the different classes, being the sensitivity and specificity values also higher than 93% in all the cases, achieving an average OA of 97.88%. Regarding the computational cost, ANNs show a higher computational cost compared with the SVM classifiers for this CS. Finally, RF also offers accurate results to differentiate between normal and tumor tissue, achieving results that outperform 89.5% of specificity and sensitivity.

Table 2. Supervised classification results in CS1

Classifier Type	#Patient	OA (%)	Sensitivity (%)	Specificity (%)	Time – 1 Fold (s)	Time – 10 Fold (s)
SVM Linear Kernel	P1	98.84	99.06	98.63	16.59	165.96
	P2	99.99	99.99	99.98	1.89	18.97
	P3	97.83	97.49	98.17	11.02	110.22
	P4	96.89	96.41	97.35	12.54	125.42
	P5	97.32	97.07	97.58	12.27	122.74
	P6	90.55	91.02	90.11	30.08	300.84
	P7	91.61	90.30	92.89	26.28	262.87
	P8	97.24	96.67	97.79	20.81	208.11
	Avg.	96.28	96.00	96.56	**16.44**	**164.39**
ANN	P1	98.79	99.00	98.58	84.35	843.57
	P2	99.99	99.99	99.99	30.05	300.56
	P3	98.94	98.93	98.95	74.71	707.19
	P4	99.05	98.71	99.38	70.66	706.62
	P5	98.23	98.33	98.12	83.07	830.75
	P6	93.75	93.11	94.37	84.41	844.17
	P7	94.37	94.49	94.26	86.04	860.47
	P8	99.91	99.89	99.93	66.64	666.43
	Avg.	**97.88**	**97.81**	**97.95**	72.49	719.97
RF	P1	97.76	98.20	97.32	27.76	277.62
	P2	99.93	99.92	99.93	16.01	160.12
	P3	96.91	96.04	97.78	27.00	270.08
	P4	98.54	98.03	99.03	23.40	234.07
	P5	95.88	95.47	96.31	28.79	287.98
	P6	91.73	91.67	91.79	38.29	382.98
	P7	90.48	89.50	91.43	39.86	398.61
	P8	99.76	99.68	99.84	20.87	208.79
	Avg.	96.37	96.06	96.68	27.75	277.53

The results achieved in the CS1 scenario shows that all the classification algorithms can reach significant classification results. The behavior measured for all the classifiers is very similar in this CS, having close averaged metrics around 96% of overall accuracy, specificity

and sensitivity. It can be observed that the classification quality also depends on the subject of study, i.e. patients #6 and #7 show lower accuracy than the other patients whatever classifiers is employed. The worst results in terms of overall accuracy are higher than 90% of success, and the values of sensitivity and specificity outperform 89.5% in all the cases. As far as computational cost is concerned, it can be seen that SVM and RF can perform the training and classification tasks more efficiently.

3.2. Case study 2

This CS aims to introduce some inter-patient variability in the classification task by merging all available data from all patients in a single data set. The model evaluation was accomplished through 10-fold cross-validation. The results achieved by all the classifiers for this CS are shown in Table 3. Although the discrimination rate in all the supervised classifiers present good discrimination capabilities to distinguish normal and tumor tissue (higher than 80% in terms of overall accuracy, sensitivity and specificity), the results have worsened compared to CS1 results. In this CS, RF and ANNs show the most competitive classification results, with values of overall accuracy, sensitivity and specificity higher than 90%. It can be also observed that the results achieved using SVM have the lowest accuracy, which metrics around 80%. The computational cost in this CS has extremely increased compared with CS1 time results due to the higher amount of data that compose the CS2 data set (more than 665,000 spectral signatures). In this CS, the computational time required for ANNs is much higher than the one required for SVM or RF. The time consumed by ANNs is almost twice than RF or SVM for training the classifier and evaluating its performance. For these reasons, RF provides more competitive prediction results, having significantly lower computational cost. Although the SVM classifier performs the classification with a lower computational cost compared to ANNs, the classification performance is slightly worst.

Table 3. Supervised classification results in CS2

Classifier Type	OA (%)	Sensitivity (%)	Specificity (%)	Time – 1 Fold (s)	Time – 10 Fold (s)
SVM Linear Kernel	82.94	86.33	79.14	**418.53**	**4185.4**
ANN	91.71	92.45	90.78	795.16	7951.6
RF	**93.25**	**93.97**	**92.35**	467.95	4679.6

3.3. Case study 3

This experimental setup reproduces a realistic situation where a pathological slide, belonging to a new patient, arrives to the Pathological Anatomy department and the prediction of the disease is performed based only on the information from previous patients. In this CS, the model evaluation is performed following a hold-out method, where the samples from a certain patient are used as a test set to evaluate the performance of the classifier model generated employing the remaining patients of the database. Patients #9 and #10 only have tumor tissue samples, so the measurement of the specificity cannot be obtained due to the impossibility of getting neither false positives nor true negatives. Therefore, the overall accuracy and the sensitivity are the same for these two patients.

Table 4 shows the classification results of each classifier per patient in the CS3 as well as the computational time results for the hold-out process. It can be seen that the classification results of this CS are not as accurate as in the other two cases. Furthermore, as it can be observed, the sensitivity and specificity values are not balanced as occurs in the other CSs. Unlike the results obtained in CS1, the prediction accuracy strongly varies between the different patients. There are some success subjects in this study, such as patients #1, #2, #3, #9 and #10, where the classification results are higher than 80% of overall accuracy. Some patients even show a classification accuracy similar to the one obtained in CS1, for instance patient #2 using the SVM classifier. Nevertheless, the models cannot be generalized enough to produce quality prediction about tissues diagnosis in the rest of the patients.

The best classification results are obtained for patient #9 where the overall accuracy and sensitivity are higher than 98% whatever classifier is employed. According to Table 4, it is possible to see that there could be chance for cross-fertilization between the different classifiers. For instance, the results obtained using SVM for patient #1 are better than 90% of overall accuracy, whereas the results for the patient #3 using this same classifier are near to 80%. Analogously, the results obtained for patient #1 in ANN is about 80% of overall accuracy, while the results for patient #3 are better (90%). Moreover, ANN achieves the best average overall accuracy (78.02%), SVM achieves the best average sensitivity (75.69%) and RF achieves the best average specificity (79.33%), demonstrating that none of the analyzed classifiers is optimum for all the patients. This fact can motivate an ensemble of supervised classifiers where the misclassifications from one classifier are compensated with the correct classification of another. Following the same trend as in the other CSs, ANNs are the classifier with the higher computational load.

Table 4. Classification results in CS3

Classifier Type	#Patient	OA (%)	Sensitivity (%)	Specificity (%)	Time (s)
SVM Linear Kernel	P1	**90.65**	**92.19**	**89.12**	468.73
	P2	**96.75**	**99.97**	**93.62**	492.41
	P3	**80.37**	**63.26**	**97.46**	457.00
	P4	66.62	66.93	65.54	426.61
	P5	57.18	62.27	51.78	381.72
	P6	38.75	21.81	54.77	349.74
	P7	81.10	74.62	87.40	428.12
	P8	58.82	90.80	28.11	413.94
	P9	**99.48**	**99.48**	-	410.59
	P10	**85.58**	**85.58**	-	474.33
	Avg.	75,53	**75.69**	70.97	**430.31**
ANN	P1	**86.51**	79.87	**93.14**	788.04
	P2	**82.48**	99.95	**65.42**	778.60
	P3	**92.48**	86.60	**98.35**	781.80
	P4	70.36	67.23	73.40	774.45
	P5	61.20	38.72	85.02	781.99
	P6	53.67	24.67	81.10	786.06
	P7	72.84	68.36	77.18	771.44
	P8	69.91	98.23	42.70	776.62
	P9	**98.73**	**98.73**	-	824.74
	P10	**92.04**	**92.04**	-	830.83
	Avg.	**78.02**	75.44	77.03	789.45
RF	P1	**80.54**	**70.35**	**90.72**	426.62
	P2	**92.18**	**99.39**	**85.15**	506.75
	P3	**8i6.46**	**73.62**	**99.28**	489.01
	P4	66.46	57.11	75.56	466.18
	P5	58.87	41.64	77.13	443.80
	P6	60.69	39.74	80.51	437.98
	P7	70.93	60.26	81.29	444.93
	P8	69.59	95.18	45.01	461.59
	P9	**99.42**	**99.42**	-	526.78
	P10	**92.70**	**92.70**	-	513.57
	Avg.	69.13	72.94	**79.33**	471.72

4. Conclusions and discussion

This research work proposes and validates several supervised classification methods to obtain an automatic diagnostic tool based on HSI to assist pathologist in the task of distinguishing between tumor and normal human brain tissue using pathological slides. For this purpose, a

customized microscopic HS acquisition system capable of capturing HS images of pathological slides in the VNIR range (from 400 nm to 1000 nm) was employed. Furthermore, a processing framework to label and classify the HS samples was established. A total of 21 diagnosed pathological slides belonging to ten different patients affected by Grade IV Glioblastoma tumor were included in this study. From these biological samples, 36 HS cubes were obtained, being labelled more than 665,000 spectral signatures of tumor and normal human brain tissue. Employing this labelled database, three different supervised classification algorithms (SVMs, ANNs and RF) were evaluated using three different case studies depending on which patients were included as subject of study.

It should be emphasized that the automatic classification of tissue will be possible once a library of spectral signatures from the different tissues have been collected according to the current diagnosis of the tissue, which have to be accomplished manually by a pathologist. This means that a lot of work is necessary to be accomplished prior to provide a real automatic diagnostic using hyperspectral image analysis. The proposed methodology is just a step forward in the achievement of automatic diagnosis tools.

The results obtained in the CS1 and CS2 experiments show competitive results in the discrimination between normal and tumor tissue, regardless of the classifier employed (achieving results above 80% of OA). The best classification results in such CSs were obtained using ANNs and RF algorithms. Comparing the results of these CSs, it is noticeable the effect of the inter-patient variability.

In the case of CS3, the classification results do not follow the same trend as in CS1 and CS2, indicating some dependence of the spectral signature with the characteristics of the patient. In half of the patients, the results are promising, while for the others the prediction error is high. The reduced number of patients involved in this study possibly causes the inaccurate results reached in CS3, since the classifier is built employing only the information from nine patients. For these reasons, it is possible that the classifiers have not enough information to build a model with higher generalization, so the model is highly biased by the patients. In future works the number of patients will be increased in order to avoid this effect. Nevertheless, this last CS delivers some promising results: for some unseen patients, it is possible to detect the tumor tissue inside pathological slides using the spectral information from previously diagnosed patients.

Regarding the computational cost of the different classifiers, ANNs is the most complex algorithm while RF and SVM have similar complexity, providing approximately a speed factor of 2x over ANNs.

In summary, HSI has proved to be a suitable technique to develop a future automatic diagnostic tool for pathological slides. Although a more exhaustive study must be carried out, including more patients and HS images with higher spectral and spatial resolution that will allow to employ more sophisticated classification schemes, this study presents promising results in the discrimination between normal and tumor brain tissue in pathological slides. Moreover, it will be possible to combine these spectral analyses with morphological ones in order to improve the overall diagnosis accuracy. In the near future, this kind of tools could help pathologist to analyze slides, speeding up the examination process of each sample.

Funding

Disclosures

The authors declare that there are no conflicts of interest related to this article.